Broadband Achromatic Metalens in the Midinfrared Range

Hongping Zhou, Lei Chen, Fei Shen, Kai Guo, and Zhongyi Guo*

School of Computer and Information, Hefei University of Technology, Hefei, 230009, China

(Received 24 August 2018; revised manuscript received 2 December 2018; published 26 February 2019)

Midinfrared devices based on metalenses are of great utility for numerous applications, including free-space communication, imaging, and molecule sensing. However, because of the intrinsic dispersion of their building bricks, metalenses significantly suffer from large chromatic aberration. In this paper, we propose an achromatic metalens that can operate over a broad band of wavelengths in the infrared region from 3.7 to 4.5 μm for circularly polarized incidences. The Pancharatnam-Berry phase and the propagation phase are used to control the wavefront of light and eliminate the chromatic aberration, respectively. As a proof-of-principle demonstration, we numerically study two devices: an achromatic focusing lens and a beam deflector. The simulation results demonstrate the devices have a focusing efficiency of about 20.7% in the infrared region from 3.7 to 4.5 μm. Our proposed approach may pave the way toward practical application of midinfrared devices.

DOI: 10.1103/PhysRevApplied.11.024066

I. INTRODUCTION

The unique ability of metasurfaces lies in their capability to control the amplitude, phase, and polarization of incident light via artificially varying nanostructures. A variety of functional optical devices based on metasurfaces have been realized covering a wide range of the spectrum from the visible region [1–3], the near-infrared region [4–6], and the midinfrared region [7–9] to the terahertz region [10–12]. In particular, the midinfrared region is of great interest for practical applications, such as free-space communication, imaging, and molecule sensing. Recently, there various midinfrared metasurface-based devices have been repoted, including metalenses [13], polarization controllers [14], modulators [15,16], perfect absorbers [17–20], vortex-beam generators [21], thermal emitters [22], nonlinear converters [23], and infrared sensors [24]. Among them, the devices based on metallic nanostructures are restricted to the reflective scheme due to the large intrinsic Ohmic loss in the midinfrared region. Therefore, dielectric metasurfaces are introduced to overcome this shortcoming [25–27], and transmissive dielectric metaoptics provide several well-established advantages in optical system design, including increased alignment tolerance and simplified on-axis configuration [25].

Almost all imaging systems suffer from chromatic aberrations, which means that light of different incident wavelengths generates focal spots at different spatial locations [28]. For metasurface devices, their chromatic aberration mainly stems from the diffractive elements, whose chromatic aberration comes mainly from the geometric arrangement of the device [29,30]. Such chromatic aberration is a serious problem in imaging system, causing degradation of imaging quality. Conventionally, chromatic aberration is eliminated by integration of several different materials with opposite dependence of the refractive index on wavelength. In contrast, metamaterials and metasurfaces provide a new paradigm for elimination of chromatic aberration by manipulating the phase, amplitude, and polarization of incident light [28,31–33]. So far, several studies have suggested the achievement of achromatic metalenses, ranging from the visible region to the near-infrared region [28,32–38]. Recently, the achromatic effect was also studied in the midinfrared region, such as reducing chromatic aberration by 55% via compensation between structure and material dispersion [39], where the peak transmissivity was 65% for 4.7–4.9 μm, and a 10×10 metalens array was used to achieve achromatic behavior at 3.2–4.1 μm with NA of 0.35 [40]. In the simulation [40], the average focusing efficiency was 70% over a wavelength range from 3 to 5 μm and the maximum focusing efficiency was 80%. However, the depth of focus of the metalens is too great compared with the wavelength. Nevertheless, it is still a great challenge to design an achromatic metalens that is able to eliminate the chromatic effect over a broad band of wavelengths in the midinfrared region.

In this paper, we propose a broadband achromatic metalens (BAML) in a transmission scheme with NA of 0.82 that eliminates the chromatic aberration over a continuous range of wavelengths from 3.7 to 4.5 μm. Our designs are based on silicon nanobricks, which stand on a CaF_2 ($n = 1.4$) substrate. We vary the length and width of the Si nanobricks to introduce the required phase compensation

*guozhongyi@hfut.edu.cn

between λ_{min} and λ_{max}. In theory, this bandwidth from λ_{min} to λ_{max} can be engineered by design of the geometric parameters, and here we choose a bandwidth with a range of 3.7–4.5 μm. As a proof-of-principle demonstration, we numerically study two devices: an achromatic focusing lens and a beam deflector. The simulation results demonstrate that the devices have an efficiency of about 20.7% at 4.5 μm.

II. THEORY, RESULTS, AND DISCUSSION

We describe the design principles for a BAML, which is schematically shown in Fig. 1(a), focusing different incident wavelengths to the same spot. A left-handed circularly polarized (LCP) beam is incident from the bottom of the substrate. The arrows with different colors indicate various incident wavelengths. Passing through the metasurfaces, the light is transformed to a right-handed circularly polarized (RCP) beam and focused at the same spot. In general, the required phase profile to achieve a focusing effect for collimated incident light is

$$\varphi(R,\lambda) = -\frac{2\pi}{\lambda}\left(\sqrt{R^2+f^2}-f\right), \tag{1}$$

where $R=\sqrt{x_0^2+y_0^2}$ is the distance from an arbitrary position (x_0, y_0) on the metalens to the center (assuming the metalens is located in the plane of $z=0$), λ is the incident wavelength, and f is the focal length. However, because of the chromatic dispersion of metasurface lenses stemming mainly from the phase-wrapping discontinuities [29], the metalens is designed to focus light of λ_{max} [Fig. 1(b)], and does not focus light of wavelength λ ($\lambda_{min} < \lambda < \lambda_{max}$) to the same focal length. Therefore, we need to modify the phase profile $\varphi(R,\lambda)$ to focus light with different wavelengths at the same position. To show the concept, the required phase profile for a BAML is schematically plotted in Fig. 1(b), where a phase difference $\Delta\varphi(R,\lambda)$ is needed for a wide range of wavelengths. λ_{min} and λ_{max} are the minimum and maximum wavelengths in the band of interest, respectively. Thus, the phase profile in Eq. (1) can be rewritten as follows: [38]:

$$\varphi_{lens}(R,\lambda) = \varphi(R,\lambda_{max}) + \Delta\varphi(R,\lambda), \tag{2}$$

with a compensation phase

$$\Delta\varphi(R,\lambda) = -\left[2\pi\left(\sqrt{R^2+f^2}-f\right)\right]\left(\frac{1}{\lambda}-\frac{1}{\lambda_{max}}\right). \tag{3}$$

Equation (2) indicates that to achieve achromatic focusing within a given bandwidth of $\Delta\lambda = \lambda_{max} - \lambda_{min}$, the required phase profile provided by an optical element can be divided into two components. The first part $\varphi(R,\lambda_{max})$ is regarded as a basic phase profile and is related to λ_{max}. The second part $\Delta\varphi(R,\lambda)$ is a function of the working wavelength and is linearly related to $1/\lambda$, which is considered as the phase difference between λ and λ_{max}. It is important to keep in mind that $\Delta\varphi(R,\lambda)$ is the key to achieve achromatic function.

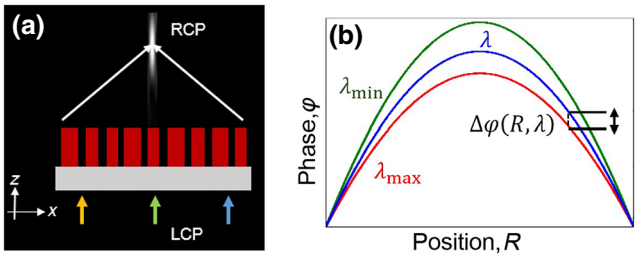

FIG. 1. (a) An achromatic metalens. The focal length is unchanged as the incident wavelength is switched, resulting in a single spot at the designed focal point for a BAML with optimized phase compensation. (b) Phase profile for a BAML at a bandwidth of $\Delta\lambda = \lambda_{max} - \lambda_{min}$.

To obtain the corresponding phase profile of $\varphi_{Lens}(R,\lambda)$, each unit element of the metalens should be artificially selected. The first term (basic phase) in Eq. (2) can be obtained by our adopting the Pancharatnam-Berry phase (PB phase). Hereafter, we introduce the design of the basic phase distribution $\varphi(R,\lambda_{max})$. As shown in Fig. 1(a), when a LCP beam passes through the nanobrick, the transmitted light can be expressed by the Jones vector [33,41]:

$$t = \frac{t_L+t_S}{2}\begin{pmatrix}1\\ i\end{pmatrix} + \frac{t_L-t_S}{2}e^{i2\alpha}\begin{pmatrix}1\\ -i\end{pmatrix}, \tag{4}$$

where t_L and t_S are complex transmission coefficients when the incident light is polarized along the long and short axes of the nanobrick, and α is the rotation angle. The first and second terms in Eq. (4) represent the copolarized and cross-polarized transmission, respectively. An additional PB phase of 2α is $\varphi(R,\lambda_{max})$ that is independent of the frequency and equal to twice the rotation angle. To acquire the phase profile of $\varphi(R,\lambda_{max})$, we use the geometric phase (PB phase) as the phase modulation in each metalens unit element. This means that we should rotate the unit elements in metasurfaces under the condition of normal LCP incidence [42].

In addition, we use the propagation phase to achieve the second term; that is, compensation-phase profile $\Delta\varphi(R,\lambda)$. In general, the propagation phase allows independent and arbitrary manipulation of phase profiles for each of two orthogonal, linear polarizations, mainly by change of the geometric parameters of the nanostructure to obtain the abrupt phase [43]. Here it is used to compensate for the required phase difference due to the dispersion of materials, as shown in Fig. 1(b). This design principle of combining the propagation phase and the PB phase

provides an opportunity to eliminate the chromatic aberration, achieving a BAML. Ideally, this principle is universal and the working bandwidth can be engineered by design of the composite materials and geometric parameters. In practice, the bandwidth will be restricted to a finite value due to limited computational ability and manufacturing difficulties.

Figure 2(a) shows the structural configuration and defines the geometric parameters. To operate efficiently in the midinfrared region, two aspects should be considered in the design of a BAML. First, a high contrast in the refractive index between the nanoscatters and their surroundings is essential for realization of enhanced manipulation of the incidence. To achieve a BAML, we use

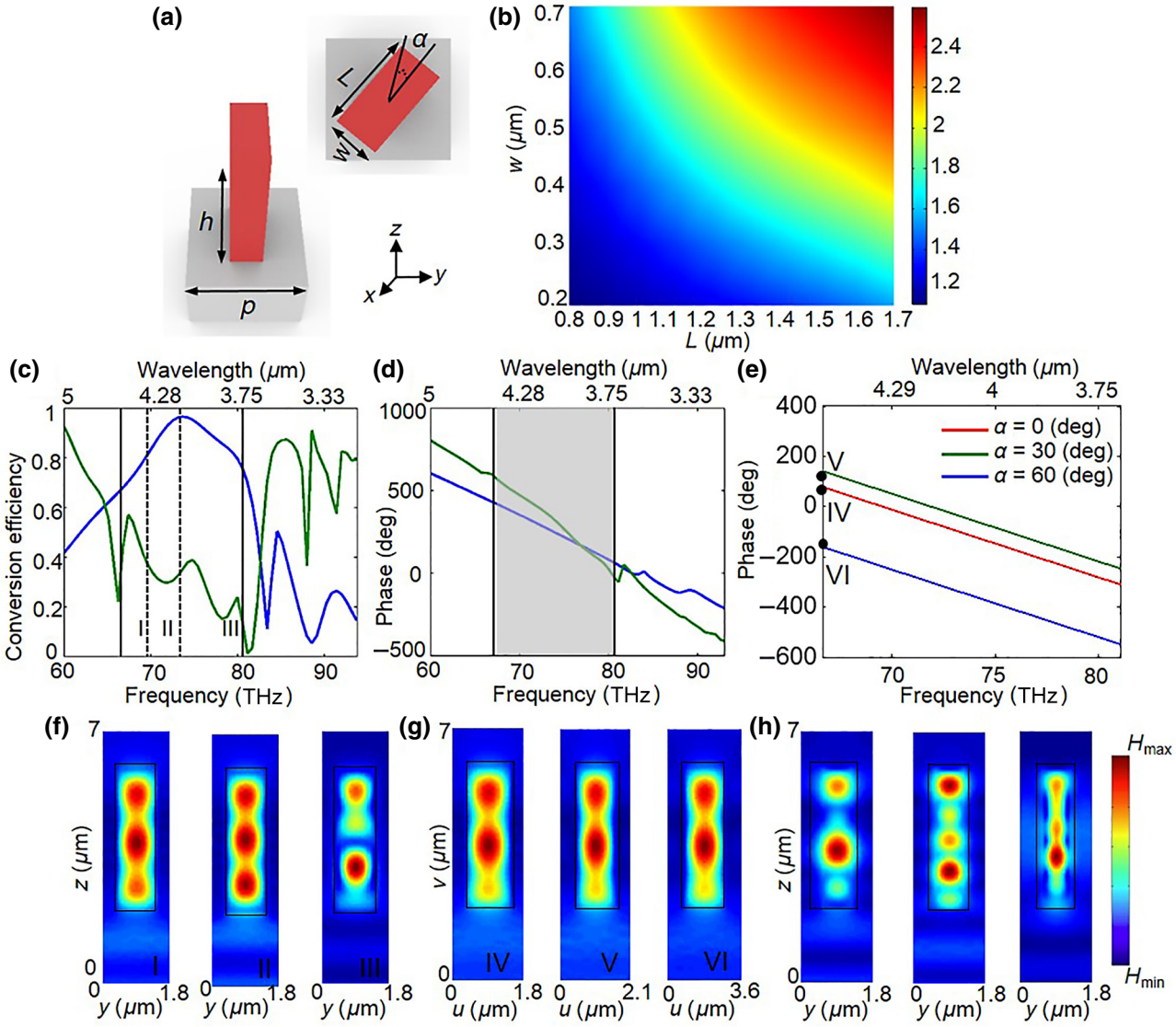

FIG. 2. A metalens element. (a) The element consists of one Si nanobrick of differing dimensions but equal height $h = 4\ \mu$m evenly spaced by a distance $p = 1.8\ \mu$m. The length L, width w, and rotation angle α are shown. The nanobrick is rotated with respect to the center of the square ($1.8 \times 1.8\ \mu$m^2). (b) The effective refractive index n_{eff} simulated by finite-element simulations of different dimensions for a Si nanobrick. LCP-to-RCP conversion efficiency (c) and phase profile (d) of two examples used in a metalens with $L = 1.2\ \mu$m and $w = 0.3\ \mu$m (blue curve) and $L = 1.3\ \mu$m and $w = 0.7\ \mu$m (green curve). (e) Phase profile as a function of frequency for different rotation angles of the nanobrick with $L = 1.2\ \mu$m and $w = 0.3\ \mu$m. The slopes of the three lines are the same; that is, the phase difference remains constant when the rotation angle changes within a given bandwidth (3.7–4.5 μm). Simulated magnetic field distribution in the y-z plane (f) and in corresponding rotated cross sections (g) at the numbers I, II, III, IV, V, and VI in (c) and (e), respectively. (u, v) represents the coordinate axis in corresponding rotated cross sections. (h) Simulated magnetic field distribution in the y-z plane at efficiency peaks (green curve) between solid black lines in (c).

silicon nanobricks since they have a high refractive index ($n = 3.429$) and negligible loss in the midinfrared region. Moreover, because of the high refractive index compared with the surrounding material, electromagnetic waves will be highly concentrated in the Si nanobricks and the coupling between neighboring nanobricks can be negligible. Therefore, we may obtain a phase difference of π between the transmission with polarization along the long and short axes of the nanobricks under the optimal conversion condition [35]. Second, materials with a low refractive index and low mid-IR absorption should be used as the substrate [7] to avoid affecting the metasurface structure. Here we chose calcium fluoride (CaF_2) for its low refractive index ($n = 1.4$) and low absorption. The Si nanobrick with height of 4 μm stands on a CaF_2 substrate with a fixed thickness of 3 μm [44]. The length and width of the nanobrick are optimized to achieve various degrees of phase compensation between λ_{max} and λ_{min}. The devices based on the Si-on-CaF_2 wafer can be experimentally fabricated by photolithography followed by reactive-ion etching [45].

We briefly describe the working principle of our proposed BAML. To eliminate chromatic aberration, we choose 14 types of element structures (summarized in Table I) satisfying the condition that the propagation phase is a linear function of $1/\lambda$. To demonstrate this, we calculate the optical property of elements 3 and 13 for wavelengths from 3.2 to 5 μm by using the finite-element method. Periodic boundary conditions are used in the x and y directions to save calculation memory and time. Perfectly matched layers are applied on boundaries in the z direction. Figure 2(c) presents the LCP-to-RCP conversion efficiency for element 3 (blue curve) and element 13 (green curve), presenting multiple resonances that are the origin of the compensation phase. Figure 2(d) shows the linear relationship between phase and frequency ($1/\lambda$) in the design wavelength range (the gray region). In addition, a required phase-compensation value can be calculated by $\Delta\varphi\,(R, \lambda)$ between λ_{max} and λ_{min}. If one needs to compensate a phase difference that equals the phase difference from 3.7 to 4.5 μm in Fig. 2(d), then either element 3 or element 13 could be used. The phase compensations achieved by the two nanobricks are 390° (blue line) and 660° (green line). Figure 2(e) shows the dependence of the propagation phase on the PB phase (i.e., rotation angle α) for the former nanobrick for different incident wavelengths. The slopes are linear and independent of the rotation angle within a given bandwidth. This means that the phase compensation implemented by the nanobrick is unchanged for different rotation angles. This property is another key to design a BAML that can operate over a large bandwidth [33].

TABLE I. Types of unit elements.

Element no.	Phase compensation (deg)	L (μm)	w (μm)
0	340	1.00	0.20
1	350	1.20	0.20
2	370	1.00	0.30
3	390	1.20	0.30
4	410	1.00	0.40
5	440	0.90	0.50
6	470	1.50	0.60
7	510	1.70	0.60
8	540	0.80	0.70
9	550	0.90	0.70
10	570	1.00	0.70
11	600	1.12	0.70
12	630	1.26	0.70
13	660	1.30	0.70

For analysis, we calculate the near-field distribution, as shown in Figs. 2(f) and 2(g). The wavelengths chosen correspond to I–VI in Figs. 2(c) and 2(e), indicating that waveguidelike cavity resonances are supported in each Si nanobrick [37]. From Fig. 2(g), it can be seen that the resonance mode is almost invariable, which explains the physical origin of the unchanged phase compensation for different rotation angles. It is worth noting that we choose relatively high nanobricks with a height of $h = 4$ μm (the working wavelength is 3.7–4.5 μm). Therefore, multiple resonances could have been excited inside the Si nanobricks to obtain a large phase compensation. A higher height is required to satisfy larger phase compensation, which causes great difficulties for experimental manufacturing. For verification, we calculate the near-field distribution of the Si nanobrick with $L = 1.3$ μm and $w = 0.7$ μm, as shown in Fig. 2(h), where the wavelengths chosen correspond to the efficiency peaks (green curve) in Fig. 2(c). From these results, compared with Figs. 2(f) and 2(g), we can see more clearly the origin of the large compensation phase comes from the multiple resonances excited in the nanobrick.

The propagation phase at a given coordinate R is $\phi(R, \lambda) = 2\pi/\lambda n_{\text{eff}} h$, where n_{eff} and h represent the effective refractive index and the height of the nanobrick, respectively. Thus, the underlying physical mechanism to obtain a large phase compensation is manipulation of n_{eff}, and n_{eff} can be expressed as $n_{\text{eff}} = k_v\lambda/2\pi$ (k_v is the axial propagation constant in Si) [46], which is closely related to the length and width of the nanobricks [46,47]. Now we describe the manipulation of n_{eff} quantitatively by reproducing the propagation constant in a Si nanobrick. In our design, the incident light is LCP light that can be decomposed into two orthogonal waveguide modes. To demonstrate this, Fig. 2(b) quantitatively shows that n_{eff} of the fundamental resonance mode increases as the dimensions of the nanobrick increase, which agrees well with waveguide theory [46]. The geometry size ranges are consistent with those used in our design and the working wavelength is 4.5 μm. Owing to the geometric symmetry, we investigate only the resonance mode where the main electric field component is parallel to the x axis. From the discussion

above, it is demonstrated that our approach has significant ability to eliminate chromatic aberration over a broadband range in the midinfrared region.

III. ACHROMATIC FOCUSING

As a proof of concept, a broadband achromatic converging metalens in the midinfrared region is designed and demonstrated. The designed BAML has a diameter of 77.4 μm with NA of 0.82. Figure 3(a) shows the simulated light-intensity profiles of the BAML in the x-z plane for incident wavelengths of 3.7, 3.9, 4.1, 4.3, and 4.5 μm. As predicted theoretically, the focal length remains almost unchanged at $f = 26$ μm (the dashed white line) within the bandwidth of interest, indicating success of the designed BAML. The inset curves represent the normalized intensity profile (divided by the maximum value in each image) along the white dashed lines at each incident wavelength. Because of the elimination of chromatic aberration, the BAML maintains its focal-spot profile for the entire spectrum from 3.7 to 4.5 μm. For comparison, the chromatic metalens has the same size as the achromatic metalens. Figure 3(b) shows the simulated light-intensity profiles of the common diffractive metalens in the x-z plane for incident wavelengths of 3.7, 3.9, 4.1, 4.3, and 4.5 μm. It is clear that the focus moves toward the common metalens with increasing wavelength. In addition, without the elimination of chromatic aberration, the normalized intensity profile along the dashed white line exhibits significant defocusing property. The shorter wavelengths in Fig. 3(a) show darker focal spots, since the transmission efficiency of the unit elements used is lower at short wavelengths than at long wavelengths.

Figure 3(c) shows the dependence of the focal length on the incident wavelength for the achromatic case (green circles) and the chromatic case (blue circles). As predicted, all focal lengths for the achromatic case remain almost unchanged when the incident wavelength varies over the bandwidth from 3.7 to 4.5 μm. In contrast to the BAML, the focal length of the chromatic metalens designed by use of the PB phase undoubtedly depends on the incident wavelength. Within the bandwidth of interest, with increasing wavelength, obvious chromatic aberration can be observed as evidenced by focal-length reduction. These results clearly demonstrate again that the BAML can eliminate the chromatic aberration effect very well. In addition, the chromatic aberration of a conventional metalens is identical to that of a diffractive lens, which can be described as [48]

$$\Delta f = f\frac{\Delta\lambda}{\lambda}, \tag{5}$$

where λ and f are the nominal (central) wavelength and focal length of the imaging system, respectively, $\Delta\lambda$ is the wavelength band over which the system operates, and Δf is the corresponding change in focal length. Substituting the corresponding parameters of the designed BAML

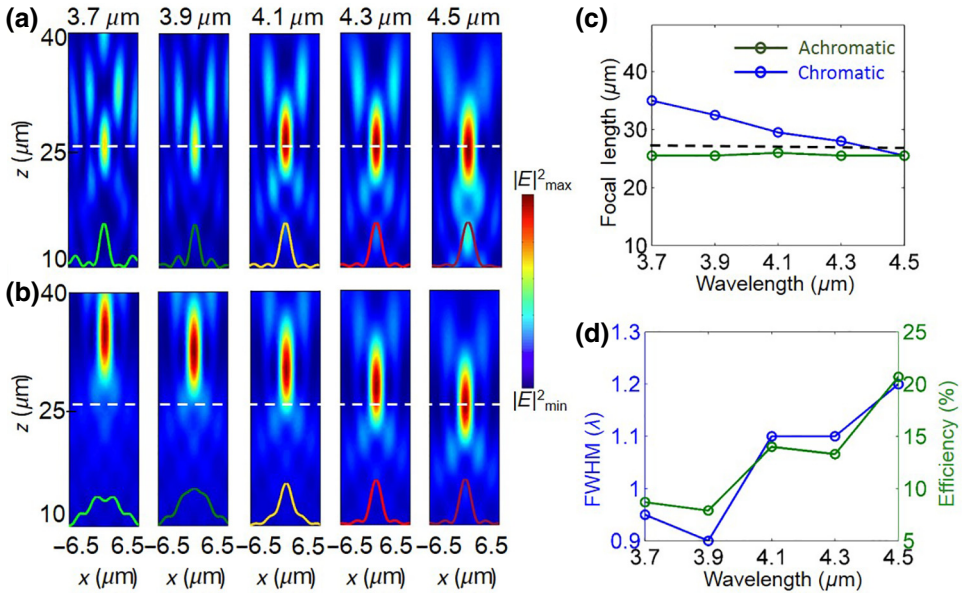

FIG. 3. Simulation results for the BAML and the chromatic metalens. Simulated intensity profiles of the focal spot in the x-z plane of (a) the designed BAML and (b) the common diffractive metalens at incident wavelengths (3.7, 3.9, 4.1, 4.3, and 4.5 μm). The inset curves show the normalized intensity profile along the dashed white line. The metalenses are designed at a basic wavelength $\lambda = 4.5$ μm with focal length $f = 27$ μm. (c) Focal lengths of the designed BAML and the chromatic metalens as a function of the incident wavelength. The dashed black line is for $f = 27$ μm. (d) The dependences of the FWHM and focusing efficiency of the designed BAML on the incident wavelength.

into Eq. (5), we can obtain $\Delta f = 4.8\ \mu$m. In contrast, the simulation results for the BAML show give $\Delta f \leq 0.5\ \mu$m, which further demonstrates the BAML can eliminate the chromatic aberration effect very well.

To further investigate the focusing performance of the designed BAML [as plotted in Fig. 3(d)], the full width at half maximum (FWHM) and the focusing efficiency are calculated at wavelengths of 3.7, 3.9, 4.1, 4.3, and 4.5 μm. The FWHM is calculated by our fitting the simulated light intensity along the focal line with a Gaussian function [38]. All calculated FWHM are in the range from 0.9λ–1.2λ. A maximum focusing efficiency (ratio of energy at the focus to incident energy) of 20.7% is achieved at $\lambda = 4.5\ \mu$m, while the efficiency decreases as the wavelength decreases. This results from the low polarization-conversion efficiency of the unit elements at short wavelength. The focusing efficiency could be further increased by optimization of the structural configuration [38].

IV. ACHROMATIC DEFLECTION

The second example we present here to demonstrate achromatic wavefront control using our proposed structures is achromatic deflection over a broadband width in the mid-IR region. The designed achromatic deflection metasurface has the ability to deflect incident light with different wavelengths over a continuous broadband wavelength range at a fixed angle. According to reported work [35] and the results above, we artificially design an array to obtain the required phase profile:

$$\varphi(x,\lambda) = \frac{2\pi}{\lambda} x \sin\theta, \tag{6}$$

where x is the spatial coordinate, λ is the wavelength, and θ is the deflected angle of the transmitted beam (i.e., the RCP-light-beam deflection under LCP incidence). To achieve achromatic deflection, the designed unit elements should satisfy the phase profile for achromatic deflection metasurfaces with a bandwidth of $\Delta\lambda = \lambda_{\max} - \lambda_{\min}$, as plotted in Fig. 4(a). Similarly, the phase profile $\varphi(x,\lambda)$ can be rewritten as follows:

$$\varphi(x,\lambda) = \varphi(x,\lambda_{\max}) + \Delta\varphi(x,\lambda) \tag{7}$$

with

$$\Delta\varphi(x,\lambda) = 2\pi x \sin\theta \left(\frac{1}{\lambda} - \frac{1}{\lambda_{\max}}\right). \tag{8}$$

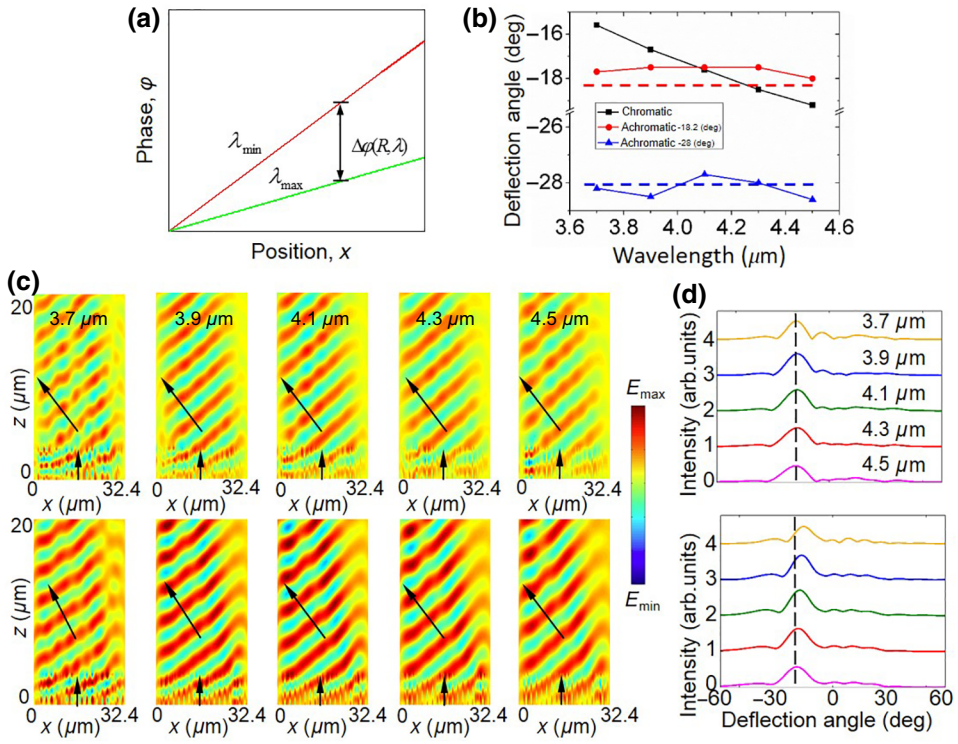

FIG. 4. Broadband achromatic deflection metasurfaces. (a) Phase profile for a broadband achromatic deflection metasurface at arbitrary incident wavelength bandwidth between $\lambda_{\min}$ and $\lambda_{\max}$. $\Delta\varphi(x,\lambda)$ expressing the phase difference within the given bandwidth. (b) The deflection angles of the designed achromatic deflector as a function of the incident wavelength. (c) The electric field distribution of the deflected RCP light under normal incidence for different wavelengths. The top panel shows the case indicated by the red circles in (b) and the bottom panel shows the case indicated by the black squares in (b). (d) Simulated deflection angle for different wavelenths of incident light from 3.7 to 4.5 μm.

To realize the phase requirement for deflection of light with an unchanged angle within the given wavelength range, the significant phase difference $\Delta\varphi\,(x,\lambda)$ needs to be taken into consideration in the design to reduce the chromatic effect, combining the PB phase to achieve the required function.

For verification, we construct two achromatic beam deflectors under normal incidence with deflection angles of -18.2° and -28° by using 18 and 19 unit elements, respectively. Figure 4(b) shows the deflection angles of the designed achromatic deflector as a function of the incident wavelength. As shown, all the RCP light is deflected at almost unchanged angles when the incident wavelength is varied from 3.7 to 4.5 μm, demonstrating a broadband achromatic performance in beam deflection. In addition, we also simulate a beam deflector without elimination of the chromatic effect, presenting significant dependence of the deflection angle on the incident wavelength, denoted by the black squares in Fig. 4(b).

Figure 4(c) displays the electric field distributions of the deflected RCP light under normal incidence with different wavelengths. The top and bottom panels show the angle offsets of the red circles and black squares in Fig. 4(b), respectively. For the achromatic case, the wavefront of the transmitted beams is deflected to almost unchanged -18.2° for incident wavelengths of 3.7, 3.9, 4.1, 4.3, and 4.5 μm, which agrees greatly with the theoretical value. In contrast, for the chromatic case, the wavefront of the transmitted beams is deflected to different oblique angles for different incident wavelengths, showing smaller angles for shorter wavelengths. Figure 4(d) shows the transmitted field intensity of RCP light as a function of the deflection angle for the achromatic deflector in the top panel and the chromatic deflector in the bottom panel, further showing the high performance of the designed achromatic deflector. Overall, the comparison between our achromatic deflector and the common one demonstrates the validity of our proposed method in designing achromatic devices in the mid-IR range. Compared with other mid-IR designs, our BAML has the advantages of light weight, small size, easy integration, and continuous broadband wavelength range. Wang *et al.* [39] designed a grating surface microstructure for chromatic aberration correction in two infrared bands of 4.7–4.9 μm and 10.5–10.7 μm. Their proposed structure is simple but with relatively narrow bandwidth compared with our proposed BAML with a broadband wavelength range of 3.7–4.5 μm. Zhang *et al.* [40] fabricated a metalens to focus light into a substrate with increased efficiency (average value of 70%) as compared with focusing light in air in normal cases. The increased efficiency resulted from the enhanced numerical aperture of the metalens in Ref. [40] in comparison with that of free space as in our designs. The results for the chromatic and achromatic cases were compared. Nevertheless, the achromatic focusing results were not discussed well as in this paper. In addition, we further investigate achromatic deflection in which the wavefront of the transmitted beam is deflected in an unchanged direction with angles of -18.2° and -28° over the broadband wavelength range of 3.7–4.5 μm. To this extent, we believe that the BAML can be useful in the development of integrated mid-IR devices.

V. CONCLUSION

In summary, we demonstrate an achromatic metalens in transmission over a continuous and broadband wavelength range in the mid-IR region by simultaneously controlling the geometric phase and phase compensation. To demonstrate this, we chose the wavelength range from 3.7 to 4.5 μm, which is limited by computing ability and can be extended further by engineering of the metasurface structure. Our metalens consists of only a single layer of nanobricks on the substrate, whose thickness is on the order of the wavelength, and does not involve spatial multiplexing or cascading. The design has an efficiency of about 20.7% at 4.5 μm, focusing light in the same focal plane in the wavelength region of interest. Through variation of the geometry of Si-based unit elements, the metasurfaces can provide corresponding phase compensation for broadband achromatic devices such as a converging metalens and a metasurface deflector. This represents a significant achievement for expanding the applications of mid-IR metalenses, which have been limited by intrinsic dispersion of the material and the geometric arrangement of the devices.

ACKNOWLEDGMENTS

This research was funded by the National Natural Science Foundation of China (Grants No. 61775050 and No. 11505043), the Natural Science Foundation of Anhui Province, China (Grants No. 1808085MF188 and No. 1808085QA21), and the Fundamental Research Funds for the Central Universities (Grants No. JD2017JGPY0005, No. JZ2018HGBZ0309, and No. JZ2018HGTB0240).

[1] J. Zhang, Z. Guo, C. Ge, W. Wang, R. Li, Y. Sun, F. Shen, S. Qu, and J. Gao, Plasmonic focusing lens based on single-turn nano-pinholes array, Opt. Express **23**, 17883 (2015).

[2] W. Wang, Z. Guo, R. Li, J. Zhang, Y. Li, Y. Liu, X. Wang, and S. Qu, Plasmonics metalens independent from the incident polarizations, Opt. Express **23**, 16782 (2015).

[3] R. Li, Z. Guo, W. Wang, J. Zhang, A. Zhang, J. Liu, S. Qu, and J. Gao, Ultra-thin circular polarization analyzer based on the metal rectangular split-ring resonators, Opt. Express **22**, 27968 (2014).

[4] A. Arbabi, Y. Horie, A. J. Ball, M. Bagheri, and A. Faraon, Subwavelength-thick lenses with high numerical apertures and large efficiency based on high-contrast transmitarrays, Nat. Commun. **6**, 7069 (2015).

[5] Z. Guo, L. Zhu, F. Shen, H. Zhou, and R. Gao, Dielectric metasurface based high-efficiency polarization splitters, RSC Adv. **7**, 9872 (2017).

[6] F. Aieta, P. Genevet, M. A. Kats, N. Yu, R. Blanchard, Z. Gaburro, and F. Capasso, Aberration-free ultrathin flat lenses and axicons at telecom wavelengths based on plasmonic metasurfaces, Nano Lett. **12**, 4932 (2012).

[7] A. Arbabi, R. M. Briggs, Y. Horie, M. Bagheri, and A. Faraon, Efficient dielectric metasurface collimating lenses for mid-infrared quantum cascade lasers, Opt. Express **23**, 33310 (2015).

[8] N. Yu, P. Genevet, F. Aieta, M. A. Kats, R. Blanchard, G. Aoust, J. P. Tetienne, Z. Gaburro, and F. Capasso, Flat optics: Controlling wavefronts with optical antenna metasurfaces, IEEE J. Sel. Top. Quantum Electron. **19**, 4700423 (2013).

[9] N. Yu, F. Aieta, P. Genevet, M. A. Kats, Z. Gaburro, and F. Capasso, A broadband, background-free quarter-wave plate based on plasmonic metasurfaces, Nano Lett. **12**, 6328 (2012).

[10] D. Hu, X. Wang, S. Feng, J. Ye, W. Sun, Q. Kan, P. J. Klar, and Y. Zhang, Ultrathin terahertz planar elements, Adv. Opt. Mater. **1**, 186 (2013).

[11] J. Zhou, J. Wang, K. Guo, F. Shen, Q. Zhou, and Z. Guo, High-efficiency terahertz polarization devices based on the dielectric metasurface, Superlattices Microstruct. **114**, 75 (2018).

[12] J. Wang, J. Zhou, K. Guo, F. Shen, Q. Zhou, and Z. Guo, High-efficiency terahertz dual-function devices based on the dielectric metasurface, Superlattices Microstruct. **120**, 759 (2018).

[13] S. Zhang, M. H. Kim, F. Aieta, A. She, T. Mansuripur, I. Gabay, M. Khorasaninejad, D. Rousso, X. Wang, M. Troccoli, N. Yu, and F. Capasso, High efficiency near diffraction-limited mid-infrared flat lenses based on metasurface reflectarrays, Opt. Express **24**, 18024 (2016).

[14] J. Park, J. H. Kang, S. J. Kim, X. Liu, and M. L. Brongersma, Dynamic reflection phase and polarization control in metasurfaces, Nano Lett. **17**, 407 (2016).

[15] N. Dabidian, I. Kholmanov, A. B. Khanikaev, K. Tatar, S. Trendafilov, S. H. Mousavi, C. Magnuson, R. S. Ruoff, and G. Shvets, Electrical switching of infrared light using graphene integration with plasmonic Fano resonant metasurfaces, ACS Photonics **2**, 216 (2015).

[16] M. C. Sherrott, P. W. Hon, K. T. Fountaine, J. C. Garcia, S. M. Ponti, V. W. Brar, L. A. Sweatlock, and H. A. Atwater, Experimental demonstration of > 230 phase modulation in gate-tunable graphene–gold reconfigurable mid-infrared metasurfaces, Nano Lett. **17**, 3027 (2017).

[17] Y. Yao, R. Shankar, M. A. Kats, Y. Song, J. Kong, M. Loncar, and F. Capasso, Electrically tunable metasurface perfect absorbers for ultrathin mid-infrared optical modulators, Nano Lett. **14**, 6526 (2014).

[18] Z. H. Jiang, S. Yun, F. Toor, D. H. Werner, and T. S. Mayer, Conformal dual-band near-perfectly absorbing mid-infrared metamaterial coating, ACS Nano **5**, 4641 (2011).

[19] T. D. Dao, K. Chen, S. Ishii, A. Ohi, T. Nabatame, M. Kitajima, and T. Nagao, Infrared perfect absorbers fabricated by colloidal mask etching of $Al - Al_2O_3$-Altrilayers, ACS Photonics **2**, 964 (2015).

[20] A. Tittl, A. K. U. Michel, M. Schäferling, X. Yin, B. Gholipour, L. Cui, M. Wuttig, T. Taubner, F. Neubrech, and H. Giessen, A switchable mid-infrared plasmonic perfect absorber with multispectral thermal imaging capability, Adv. Mater. **27**, 4597 (2015).

[21] N. Yu, P. Genevet, M. A. Kats, F. Aieta, J. P. Tetienne, F. Capasso, and Z. Gaburro, Light propagation with phase discontinuities: Generalized laws of reflection and refraction, Science **334**, 1210713 (2011).

[22] D. Costantini, A. Lefebvre, A. L. Coutrot, I. Moldovan-Doyen, J. P. Hugonin, S. Boutami, F. Marquier, H. Benisty, and J. J. Greffet, Plasmonic Metasurface for Directional and Frequency-selective Thermal Emission, Phys. Rev. Appl. **4**, 014023 (2015).

[23] J. Lee, N. Nookala, J. S. Gomez-Diaz, M. Tymchenko, F. Demmerle, G. Boehm, M. C. Amann, A. Alù, and M. A. Belkin, Ultrathin second-harmonic metasurfaces with record-high nonlinear optical response, Adv. Opt. Mater. **4**, 664 (2016).

[24] Z. Wu, G. Kelp, M. N. Yogeesh, W. Li, K. M. McNicholas, A. Briggs, B. B. Rajeeva, D. Akinwande, S. R. Bank, G. Shvets, and Y. Zheng, Dual-band moiré metasurface patches for multifunctional biomedical applications, Nanoscale **8**, 18461 (2016).

[25] L. Zhang, J. Ding, H. Zheng, S. An, H. Lin, B. Zheng, Q. Du, G. Yin, J. Michon, Y. Zhang, Z. Fang, M. Shalaginov, L. Deng, T. Gu, H. Zhang, and J. Hu, Ultra-thin high-efficiency mid-infrared transmissive Huygens meta-optics, Nat. Commun. **9**, 1481 (2018).

[26] S. Jahani, and Z. Jacob, All-dielectric metamaterials, Nat. Nanotechnol. **11**, 23 (2016).

[27] Z. Guo, L. Tian, F. Shen, H. Zhou, and K. Guo, Mid-infrared polarization devices based on the double-phase modulating dielectric metasurface, J. Phys. D: Appl. Phys. **50**, 254001 (2017).

[28] P. Wang, N. Mohammad, and R. Menon, Chromatic-aberration-corrected diffractive lenses for ultra-broadband focusing, Sci. Rep. **6**, 21545 (2016).

[29] E. Arbabi, A. Arbabi, S. M. Kamali, Y. Horie, and A. Faraon, Multiwavelength polarization-insensitive lenses based on dielectric metasurfaces with meta-molecules, Optica **3**, 628 (2016).

[30] E. Arbabi, A. Arbabi, S. M. Kamali, Y. Horie, and A. Faraon, Controlling the sign of chromatic dispersion in diffractive optics with dielectric metasurfaces, Optica **4**, 625 (2017).

[31] K. Guo, J. Liu, Y. Zhang, and S. Liu, Chromatic aberration of light focusing in hyperbolic anisotropic metamaterial made of metallic slit array, Opt. Express **20**, 28586 (2012).

[32] F. Aieta, M. A. Kats, P. Genevet, and F. Capasso, Multiwavelength achromatic metasurfaces by dispersive phase compensation, Science **347**, 1342 (2015).

[33] W. T. Chen, A. Y. Zhu, V. Sanjeev, M. Khorasaninejad, Z. Shi, E. Lee, and F. Capasso, A broadband achromatic metalens for focusing and imaging in the visible, Nat. Nanotechnol. **13**, 220 (2018).

[34] S. Colburn, A. Zhan, and A. Majumdar, Metasurface optics for full-color computational imaging, Sci. Adv. **4**, eaar2114 (2018).

[35] H. H. Hsiao, Y. H. Chen, R. J. Lin, P. C. Wu, S. Wang, B. H. Chen, and D. P. Tsai, Integrated resonant unit of metasurfaces for broadband efficiency and phase manipulation, Adv. Opt. Mater. **6**, 1800031 (2018).

[36] M. Khorasaninejad, Z. Shi, A. Y. Zhu, W. T. Chen, V. Sanjeev, A. Zaidi, and F. Capasso, Achromatic metalens over 60 nm bandwidth in the visible and metalens with reverse chromatic dispersion, Nano Lett. **17**, 1819 (2017).

[37] S. Wang, P. C. Wu, V. C. Su, Y. C. Lai, M. K. Chen, H. Y. Kuo, B. H. Chen, Y. H. Chen, T. T. Huang, J. H. Wang, R. M. Lin, C. H. Kuan, T. Li, Z. Wang, S. Zhu, and D. P. Tsai, A broadband achromatic metalens in the visible, Nat. Nanotechnol **13**, 227 (2018).

[38] S. Wang, P. C. Wu, V. C. Su, Y. C. Lai, C. H. Chu, J. W. Chen, S. H. Lu, J. Chen, B. Xu, C. H. Kuan, T. Li, S. Zhu, and D. P. Tsai, Broadband achromatic optical metasurface devices, Nat. Commun. **8**, 187 (2017).

[39] J. Wang, Y. Sun, X. Ji, L. Wang, Y. Wang, and Z. Li, Research on grating surface microstructure for the chromatic aberration compensation in infrared band, Infrared Phys. Technol. **92**, 280 (2018).

[40] S. Zhang, A. Soibel, S. A. Keo, D. Wilson, S. Rafol, D. Z. Ting, A. She, S. D. Gunapala, and F. Capasso, Solid-immersion metalenses for infrared focal plane arrays, arXiv:1805.06608 (2018).

[41] N. Yu, and F. Capasso, Flat optics with designer metasurfaces, Nat. Mater. **13**, 139 (2014).

[42] M. Kang, T. Feng, H. T. Wang, and J. Li, Wave front engineering from an array of thin aperture antennas, Opt. Express **20**, 15882 (2012).

[43] J. B. Mueller, N. A. Rubin, R. C. Devlin, B. Groever, and F. Capasso, Metasurface Polarization Optics: Independent Phase Control of Arbitrary Orthogonal States of Polarization, Phys. Rev. Lett. **118**, 113901 (2017).

[44] C. Yu, L. Hongtao, H. Juejun, and L. Mo, Heterogeneously integrated silicon photonics for the mid-infrared and spectroscopic sensing, ACS Nano **8**, 6955 (2014).

[45] R. Dharmavarapu, S. H. Ng, S. Bhattacharya, and S. Juodkazis, in *Nanophotonics Australasia 2017* (International Society for Optics and Photonics, Melbourne, Australia, 2018), Vol. 10456, p. 104561W.

[46] E. A. Marcatili, Dielectric rectangular waveguide and directional coupler for integrated optics, Bell Syst. Tech. J. **48**, 2071 (1969).

[47] E. Schonbrun, K. Seo, and K. B. Crozier, Reconfigurable imaging systems using elliptical nanowires, Nano Lett. **11**, 4299 (2011).

[48] J. Engelberg, and U. Levy, Optimizing the spectral range of diffractive metalenses for polychromatic imaging applications, Opt. Express **25**, 21637 (2017).